



Benefits of fully focused SAR altimetry to coastal wave height estimates: A case study in the North Sea

Florian Schlembach^{a,*}, Frithjof Ehlers^b, Marcel Kleinherenbrink^b, Marcello Passaro^a,
Denise Dettmering^a, Florian Seitz^a, Cornelis Slobbe^b

^a Deutsches Geodätisches Forschungsinstitut, Technical University of Munich (DGFI-TUM), Arcisstraße 21, Munich, 80333, Germany

^b Geoscience and Remote Sensing, Delft University of Technology, Stevinweg 1, Delft, 2628 CN, The Netherlands

ARTICLE INFO

Edited by Menghua Wang

Keywords:

Satellite altimetry
SAR altimetry
FF-SAR
Fully focused SAR
UF-SAR
Unfocused SAR
Sentinel-6 Michael Freilich
Significant wave height
Retracking
Coastal retracking
Coastal zone
Algorithm
SAMOSA
CORAL
Case study
North sea
SWH decay
Coastal SWH variation

ABSTRACT

Estimating the three geophysical variables significant wave height (SWH), sea surface height, and wind speed from satellite altimetry continues to be challenging in the coastal zone because the received radar echoes exhibit significant interference from strongly reflective targets such as sandbanks, sheltered bays, ships etc. Fully focused SAR (FF-SAR) processing exhibits a theoretical along-track resolution of up to less than half a metre. This suggests that the application of FF-SAR altimetry might give potential gains over unfocused SAR (UF-SAR) altimetry to resolve and mitigate small-scale interferers in the along-track direction to improve the accuracy and precision of the geophysical estimates.

The objective of this study is to assess the applicability of FF-SAR-processed Sentinel-6 Michael Freilich (S6-MF) coastal altimetry data to obtain SWH estimates as close as possible to the coast.

We have developed a multi-mission FF-SAR processor and applied the coastal retracking algorithm CORALv2 to estimate SWH. We assess different FF-SAR and UF-SAR processing configurations, as well as the baseline Level-2 product from EUMETSAT, by comparison with the coastal, high-resolution SWAN-Kuststrook wave model from the Deltares RWsOS North Sea operational forecasting system. This includes the evaluation of the correlation, the median offset, and the percentage of cycles with high correlation as a function of distance to the nearest coastline. Moreover, we analyse the number of valid records and the L2 noise of the records. The case study comprises five coastal crossings of S6-MF that are located along the Dutch coast and the German coast along the East Frisian Islands in the North Sea.

We observe that accurate and precise SWH records can be estimated in the nearshore zone within 1–3 km from the coast using satellite SAR altimetry. We find that the FF-SAR-processed dataset with a Level-1b posting rate of 140 Hz shows the greatest similarity with the wave model. We achieve a correlation of ~0.8 at 80% of valid records and a gain in precision of up to 29% of FF-SAR vs UF-SAR for 1–3 km from the coast. FF-SAR shows, for all cycles, a high correlation of greater than or equal to 0.8 for 1–3 km from the coast. We estimate the decay of SWH from offshore at 30 km to up to 1 km from the coast to amount to $26.4\% \pm 3.1\%$.

1. Introduction

The knowledge of wave heights in the open ocean is relevant for ocean weather forecasting (Cavaleri et al., 2012), climate studies (Timmermans et al., 2020; Stopa et al., 2016), scientific studies such as for the air–sea interactions of surface-breaking waves (Melville, 1996), as well as for applications such as industrial shipping route planning. Furthermore, wave heights in the coastal zone are of particular interest as about 23%–37% of the world's population lives within 100 km of the shoreline (Glavovic et al., 2022). This is especially true for coastal risk assessment studies (Ferreira et al., 2009; Sajjad and Chan,

2019), coastal protection (Pilarczyk, 1990; Charlier et al., 2005), and coastal safety (Arens et al., 2013). Moreover, there are high demands to measure wave heights even closer to the coast, e.g. for studying nearshore effects such as wave energy transformation (Lippmann et al., 1996; Contardo et al., 2018), sediment transport (Elfrink and Baldock, 2002; Chowdhury and Behera, 2017; de Vries et al., 2020), dissipation effects (Wright, 1976; Wang and Kraus, 2005; Bryan and Power, 2020).

One way to measure wave heights globally is with satellite radar altimetry, which has been in use for over three decades to obtain

* Corresponding author.

E-mail addresses: florian.schlembach@tum.de (F. Schlembach), f.ehlers@tudelft.nl (F. Ehlers), m.kleinherenbrink@tudelft.nl (M. Kleinherenbrink), marcello.passaro@tum.de (M. Passaro), denise.dettmering@tum.de (D. Dettmering), florian.seitz@tum.de (F. Seitz), d.c.slobbe@tudelft.nl (C. Slobbe).

<https://doi.org/10.1016/j.rse.2023.113517>

Received 27 November 2022; Received in revised form 26 January 2023; Accepted 21 February 2023

Available online 6 March 2023

0034-4257/© 2023 Elsevier Inc. All rights reserved.

estimates of sea level and sea state. The measurement principle of satellite radar altimetry is based on measuring the echoes of a transmitted frequency-modulated pulse as a function of two-way travel time. From the shape of the returned/received and processed pulse echoes and their amplitudes, the three geophysical variables sea surface height (SSH), significant wave height (SWH), and wind speed can be derived in a process called retracking, in which a model is fit to the received pulse echoes. The SWH is defined as four times the standard deviation of the sea surface elevation (Holthuijsen, 2007). The most recent operational satellite altimetry processing is called unfocused synthetic aperture radar (UF-SAR)/Delay-Doppler (DD) processing (Raney, 1998), which is applied to the satellite altimetry missions CryoSat-2 (CS2), Sentinel-3 (S3), and Sentinel-6 Michael Freilich (S6-MF).

Measuring wave heights in the coastal zone using satellite altimetry is challenging due to complex processes occurring near the coast, which triggered the emergence of the relatively new research field of coastal altimetry (Vignudelli et al., 2011). Numerous works have addressed the challenges of coastal altimetry (Fenoglio-Marc et al., 2010; Vignudelli et al., 2011; Cipollini et al., 2009, 2012; Gomez-Enri et al., 2016). Timmermans et al. (2020) assessed extreme wave heights from satellite altimetry, which agree well with in-situ data for up to 5 km from the coast but lack proper spatio-temporal sampling for closer distances to the coast. Coastal SWH observations from satellite altimetry are often discarded or are of bad quality due to coastal interference that originates from strongly reflective targets such as sandbanks, sheltered bays, or calm waters close to the shoreline. Schlembach et al. (2022) showed that the correlation of SWH data of the operational baseline product of S3 with in-situ data from buoys amounts to less than 0.20 for closer than 20 km from the coast. Tailored retracking algorithms have been developed to account for the coastal interference, such as ALES (Passaro et al., 2015), Brown-Peaky (Peng and Deng, 2018) for the conventional low resolution mode (LRM) altimetry, and SAMOSA+ (Dinardo et al., 2018), SAMOSA++ (Dinardo et al., 2020), ALES + SAR (Passaro et al., 2021), RiwiSAR-SWH (Gou and Tourian, 2021), CORS (Garcia et al., 2022), or CORALv1 (Schlembach et al., 2022) for UF-SAR altimetry. The enhanced coastal processing algorithms allow the derivation of relevant wave-related statistics in the coastal zone, e.g. as done by Passaro et al. (2021). They investigated the global attenuation of SWH from offshore at 30 km to >3 km off the coast and found the wave heights are globally, on average, 22% smaller than offshore while using the conventional LRM altimetry with a lower posting rate of 1 Hz (and the ALES retracker (Passaro et al., 2015)). The estimation of SWH in the coastal zone with a distance-to-coast (dist-to-coast) of <5 km remains challenging, as the quality of the estimates deteriorates (Schlembach et al., 2022). Nevertheless, the need to approach the coastline even closer is specified by the current draft of the mission requirement documents of the Copernicus Sentinel-3 Next Generation Topography (S3NG-T) team, which has defined the requirement to give SSH and SWH estimates up to 3 km and, as an enhanced target, up to 0.5 km off the coastline (European Space Agency and Noordwijk, The Netherlands, 2022).

As an evolution of UF-SAR altimetry, fully focused synthetic aperture radar (FF-SAR) altimetry constitutes a novel processing technique initially applied to altimetry data by Egidio and Smith (2017). It exploits the fully coherent processing of the received radar pulse echoes during the whole target illumination time, by which a theoretical along-track resolution of less than a meter can be achieved for coherent targets. With FF-SAR processing, we expect to acquire SWH estimates that are less affected by strongly reflective targets in the coastal zone due to its inherently high along-track resolution.

The S6-MF mission offers great potential to apply FF-SAR processing due to its open-burst, interleaved operation mode, i.e. the pulses are continuously transmitted and received in a manner that the reception of the pulses occurs in between the phases of transmission (Donlon et al., 2021). That is, only minor spurious grating lobes (or: target replicas) are expected in the along-track direction at multiples of ~300 m (Ehlers

et al., 2022), as compared to the CS2 or S3 missions that exhibit more frequent and stronger grating lobes at ~90 m (Egidio and Smith, 2017; Guccione et al., 2018) due to the lacunar sampling/closed-burst operation mode.

This work is a case study to assess the capability of FF-SAR-processed S6-MF coastal altimetry data to obtain SWH estimates as close as possible to the coastline.

In order to achieve this, we formulate the following research objectives:

1. We aim to assess whether the SWH estimation from coastal altimetry data can be further improved by using FF-SAR instead of UF-SAR processing.
2. Furthermore, we want to evaluate whether the statistical improvements observed in the coastal SWH estimates are also beneficial in practice for determining key metrics that are relevant for fields such as coastal protection.

To address both, we aim to perform a(n)

- Comparison of the FF-SAR- and UF-SAR-processed altimetry data with a high-resolution wave model data as a function of dist-to-coast
- Evaluation of the number of valid records and the precision of the altimetry data as a function of dist-to-coast
- Identification and quantification of dissimilarities between the altimetry data and high-resolution wave model data
- Exploitation of nearshore SWH records by the estimation of the change in SWH from offshore towards to the coast

To the best knowledge of the authors, no previous study is known that has performed such an in-depth assessment of FF-SAR-processed wave data estimated by a satellite altimeter.

This paper is structured as follows: Section 2 describes the altimetry and wave model data used. Section 3 explains the processing chain of the altimetry data, the methods to compare the altimetry datasets with the wave model and the estimation of the number of valid records and precision of the altimetry estimates, as well as the metric of the coastal SWH variation. Section 4 presents and discusses the results of the study. Section 5 draws a conclusion and gives an outlook for future work.

2. Data

2.1. Altimetry

We use S6-MF Level-1a (L1a) and Level-2 (L2) data baseline version F06 in the Non Time Critical (NTC) timeliness. The data was downloaded using the PO.DAAC interface from the NASA Jet Propulsion Laboratory (NASA JPL, 2020). We process the L1a data to acquire two FF-SAR- and one UF-SAR-processed datasets. The processing chain and the settings of the datasets will be described in detail in Section 3.1. In addition, we take the Payload Data Acquisition and Processing High Resolution (PDAP-HR) dataset from the baseline L2 products, which corresponds to the baseline UF-SAR/HR processing chain as described in the S6-MF L2 product generation specification document (EUMETSAT, 2022b). The PDAP-HR dataset is retracked with the open ocean SAMOSA-based retracker (EUMETSAT, 2022b, Section 4.5.2), which is not optimised for the coastal zone. We, though, include it as a reference to highlight the improvements to the SWH estimates by our processing configurations. The provided `swh_ocean_qual` flag is used to exclude bad estimates. The residual estimates represent the number of valid records, which are part of our statistical analysis. For the discussion of the offset with respect to the wave model, we also include the Payload Data Acquisition and Processing Low Resolution (PDAP-LR) product from the baseline L2 product, which is processed according to the LR processing chain (EUMETSAT, 2022b, Section 4.5.1).

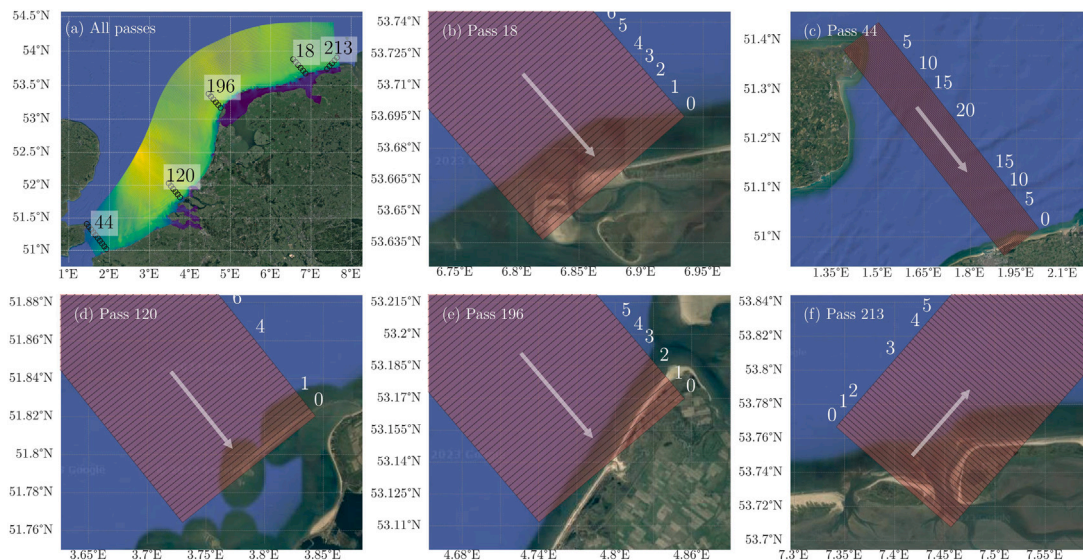


Fig. 1. The model domain of the SWAN-Kuststrook wave model with its curvilinear grid is shown in (a). Panels b, c, d, e and f display the S6-MF passes 44, 120, 196, 18, and 213, respectively. The white numbers next to each pass indicate the dist-to-coast values, and the white arrows show the flight direction of the satellite. The estimated effective footprints have a size of 300×10000 m (along-track times across-track) and comprise the area on the ground that is estimated to have a major impact on the leading edge (LE) of the multilooked waveform, i.e. on the estimates of the geophysical variables.

We use all available S6-MF data of the year 2021 included in the wave model domain (see next section), which corresponds to cycles 5 to 42 and the five passes 18, 44, 120, 196, and 213. All passes apart from 213 are descending, and, in total, 161 overpasses are available. Measurements from up to 31 km from the coast are included. The rationale behind not encompassing a much larger area from the coast is to limit the computational effort that is inherently large to FF-SAR processing that uses the back-projection algorithm. The dist-to-coast range was thus chosen to be large enough to accommodate the computation of the coastal SWH variation with respect to the offshore SWH around 30 km. We define the outermost contact of the satellite's nadir locations with land as the coastline to avoid the tidal flats of the Wadden Sea. A map of the collocated data is shown in Fig. 1 (a). Fig. 1 (b–f) shows the zoomed-in views of the five individual coastal crossings.

Below is a description of the five S6-MF passes analysed in this study.

Pass 18 goes over the western tip of the Wadden island Juist, Germany. The first two kilometres off the coast are covered by sandbanks, which deteriorates the accuracy and the validity of the records due to the strongly reflective characteristic of sandbanks.

Pass 44 crosses over the English Channel, where the satellite passes the UK shoreline with a minimum distance of ~ 2 km and goes south to the French north coast close to Calais and thus comprises two coastal areas. The pass is located on the southwestern edge of the wave model domain. The angle of approach to the coast in the south amounts to approximately 60° (90° would mean a perpendicular crossing).

Pass 120 is a coastal crossing located south of Rotterdam. The pass almost perpendicularly crosses a large sandbank called Aardappelenbult. The dist-to-coast is manually set to 0.0 km at the outer edge of the sandbank. This segment of the pass is quite a special coastal crossing, as no land intrusion is apparent for the very last radar footprints.

Pass 196 is the coastal crossing of the Dutch Wadden island Texel. The angle of approach to the coastline is slightly tilted ($\sim 108^\circ$) such that the footprints of the first 1–2 km off the coast are affected by land intrusion.

Pass 213 crosses the East Frisian Wadden island Baltrum, Germany. Its effective radar footprints are affected by many strongly reflective targets such as sandbanks, inland waters, and land/human infrastructure.

2.2. SWAN-Kuststrook wave model

To assess the potential of FF-SAR-processed S6-MF coastal altimetry data in the SWH estimation, we compared it with model-derived data. We are aware that wave model data cannot be considered the truth. However, it represents a practical way to evaluate the variability of SWH on a fine scale, such as spatial variations towards the coast, whereas buoys, which are mostly not located at the coast, can only provide pointwise measurements with limited resolution in space and time. We use the SWAN-Kuststrook wave model, which is part of the Deltares RWsOS North Sea operational forecasting system. Simulating Waves Nearshore (SWAN) is a third-generation wave model that simulates random, short-crested wind-waves in coastal regions (Booij et al., 1999) and is developed at the Delft University of Technology. It represents wave evolutions due to wind, white-capping, shoaling, bottom friction, current and depth-induced refraction, diffraction, depth-induced breaking and quadruplet/triad wave-wave-interactions (Day and Dietrich, 2022). The output of the SWAN-Kuststrook wave model is generated by the SWAN software version 41.20A.2, which includes a new set of wave physics (ST6) for the parametrisation of wind input and wind speed scaling, swell dissipation, white-capping, and others (Rogers et al., 2012). The model domain with a snapshot of SWH data is shown in Fig. 1 (a) and encompasses the Dutch North Sea, the Dutch Wadden Sea, the Eastern and Western Scheldt, and the German North Sea along the East Frisian Islands. It is a nested model; the boundary conditions are taken from the regional ECMWF-WAM model that has a 0.1° geographical resolution (Janssen, 2011). The water level and current fields come from runs of the hydrodynamic model WAQUA-ZUNO (Gautier and Caires, 2015) and the wind fields from the High Resolution Limited Area Model (HIRLAM) (Undén et al., 2002). The bathymetry data is computed from EMODnet (EMODnet Bathymetry Consortium, 2018) and Baseline-NL (National Georegister of the Netherlands, 2021) datasets for the deeper parts and near the coast, respectively. The model grid is curvilinear and comprises 991 times 310 points. The grid spacing in the longitudinal and latitudinal directions ranges from 50–1400 m

Table 1

L2 datasets used in this study. FFSAR-60 and FFSAR-140 are averaged after the retracking to form L2 estimates at a posting rate of 20 Hz, as described in Section 3.1.2. The PDAP-HR and PDAP-LR datasets are taken from the EUMETSAT baseline L2 product.

Name	L1b: proc. type	L1b: posting rate [Hz]	L2: retracker
FFSAR-60	FF-SAR	60	CORALv2
FFSAR-140	FF-SAR	140	CORALv2
UFSAR-20	UF-SAR	20	CORALv2
PDAP-HR	UF-SAR	20	SAMOSa-based
PDAP-LR	LRM	20	MLE4

and 35–2600 m, respectively, with the closest grid points being located near the coast to resolve small-scale dynamics. An assessment of the performance of the SWAN-Kuststrook wave model was conducted with in-situ observations data from 50 different locations. The performance was compared to the previously operational SWAN-ZUNO model within a hindcast-based analysis of four extreme events, which yields a relative bias of -1% (SWAN-ZUNO: -12%) and a scatter index of 23% (SWAN-ZUNO: 22%) for the SWH. The extreme event analysis also comprises phases with low sea states, from which we conclude that the model shows a comparably good performance also for these sea state regimes.

We compare the altimetry- and model-derived data at the locations from the EUMETSAT baseline L2 high-resolution product. The wave model data is mapped to the baseline L2 locations using a bilinear interpolation.

3. Methods

In this section, we first describe the processing methodology of the altimetry data starting from the L1a product and ending with the SWH estimates (L2 product). Secondly, we describe the statistical analysis to assess the performance of all L2 datasets. Thirdly, we explain the evaluation of the coastal SWH variation of the L2 datasets towards the coastline.

3.1. Processing of altimetry data

Here, we describe the details of the Level-1b (L1b) processing, starting from the received pulses and ending in the multilooked power return echo waveforms, from which the three geophysical variables SWH, SSH, and wind speed are estimated in the L2 processing stage, as described in Section 3.1.2. Table 1 lists and summarises the key properties of all datasets used in this study.

3.1.1. Level-1b processing

We process the received pulse echoes from the L1a products to acquire the return power waveforms at the L1b data level. This is established using a multi-mission FF-SAR processor implementation originally developed for CS2 by Kleinherenbrink et al. (2020), which applies a back-projection algorithm as presented in Egido and Smith (2017). The extension to the S3 and S6-MF missions is described in detail in Ehlers et al. (2022). The FF-SAR processing includes the range cell migration correction (RCMC), the residual video phase (RVP) correction, and the compensation for additional phase jumps and other mission-specific settings (Ehlers et al., 2022). Here, we describe only specific FF-SAR processing parameters that are used for this study and are summarised in Table 2.

The FF-SAR processor obtains a statistically independent, singlelook waveform every ~ 1 m in the along-track direction while setting a coherent integration time $T = 2.1$ s. The specific setting of $T = 2.1$ s has been evaluated to be the most sensitive within the ESA L2 GPP project (European Space Agency and Noordwijk, The Netherlands, 2021). The singlelook waveforms are averaged in a process called multilooking, in which non-overlapping singlelook waveforms are averaged to form multilooked waveforms in distances that correspond to the

Table 2

L1b processing parameters used for the FFSAR-60, FFSAR-140, and UFSAR-20 datasets.

Parameter	Value
Illumination time T	2.1 s (FF-SAR)/2.4 s (UF-SAR)
Zero-padding-factor	2
Number of range gates N_r	512
L1b posting rate	FF-SAR: 60/140 Hz, UF-SAR: 20 Hz
Window applied	None

targeted 60 Hz and 140 Hz L1b posting rates. Both 60 and 140 Hz are odd-numbered multiples of 20 Hz (three and seven) so that the centre of the averaged 60 Hz and 140 Hz measurements can be georeferenced to the 20 Hz records of the baseline L2 product.

The UF-SAR-processed L1b products are a by-product of the same FF-SAR processor, which allows us to mimic the original DD/SAR processing chain Dinardo et al. (2018). The time for the coherent integration of the (range- and phase-corrected) pulses of each individual burst is reduced from the illumination time T to the burst duration, which is different from FF-SAR, where all pulses over T are coherently integrated. This reduces the theoretical along-track resolution from ~ 1 m to ~ 300 m, assuming a static scenario of scatterers within T (Egido and Smith, 2017). The chosen illumination time of $T = 2.4$ s corresponds to the number of looks (or Doppler beams) of 322 to be in line with the baseline PDAP product (EUMETSAT, 2022a). The Doppler-beam stack is acquired by taking the absolute square of the integrated bursts, from which the UF-SAR-multilooked waveform (as part of the PDAP-HR L1b product) is obtained through summation over all bursts. We can thus collect (correlated) UF-SAR-multilooked waveforms every ~ 1 m along with each of the FF-SAR-singlelooks (Egido et al., 2020). After picking the multilooked waveforms at locations that are nearest to the ones of the EUMETSAT baseline L2 product, we acquire the UFSAR-20 dataset, which closely matches the baseline PDAP-HR product (after the averaging as explained in the next paragraph), but excluding the spurious range-walk error, as investigated by Guccione (2008) and Scagliola et al. (2021). Some authors report an increased precision by averaging consecutive UF-SAR from 40 Hz or 60 Hz posting rates onto 20 Hz (Dinardo et al., 2015; Egido et al., 2020). However, we find that this step introduces a correlation between neighbouring 20 Hz records and is thus not considered as viable option; see Appendix A. Hence, an apparent gain in precision might, in part, be caused by the effective low-pass filtering of the geophysical estimates and a corresponding loss in resolution, which is not desired.

3.1.2. Level-2 processing

The FF-SAR- and UF-SAR-processed L1b multilooked power waveforms are retracked with the COastal Retracker for SAR Altimetry version 2.0 (CORALv2) algorithm to extract the SWH data, as presented in its first version, v1, in Schlembach et al. (2022) (details on differences below). As commonly done for the retracking algorithms, CORALv2 performs a least-squares fitting of the theoretical waveform, the SAMOSA2 model, with the received, multilooked waveforms and extracts the ocean parameters SWH, SSH, and wind speed. The SAMOSA2 model is an analytical formulation of the power return echoes. It takes into account instrument-specific (e.g. pulse repetition frequency, carrier frequency, transmission and reception bandwidths) and orbital parameters such as the altitude, altitude rate, and velocity. In its analytical form, it makes several approximations, such as the Gaussian approximation of the point target response (PTR) (Ray et al., 2015). In order to account for these, a sea-state-dependent look-up table (LUT) is used for the α_p value that is part of the analytical SAMOSA2 model. The approximations depend, amongst others, on the illumination time T and also the coherent integration time used in the L1b processing. Hence, we use the α_p LUT from the PDAP baseline (EUMETSAT, 2022a) for the UF-SAR waveforms, whose illumination time is chosen to be 2.4 s (corresponding to 322 looks) and the coherent

integration time to be the burst repetition interval (BRI) (as for the PDAP-HR product). For FF-SAR, an α_p LUT is generated considering an illumination time of $T = 2.1$ s and assuming an unambiguous PTR, i.e. no grating lobes (or azimuth-ambiguities) of the PTR are taken into account (pers. comm. Salvatore Dinardo). This tailored α_p LUT is then used to fit the SAMOSA zero-Doppler beam against the waveform, as initially presented in [Egido and Smith \(2017\)](#).

CORALv2 is based on SAMOSA+ ([Dinardo et al., 2018](#)) and adds further extensions to mitigate interference that arises from strongly reflective targets in the across-track direction, as is typical in the coastal zone. Furthermore, a better quality flag allows for an over 25% increase in valid estimates closer than 5 km from the coast compared to SAMOSA+ ([Schlembach et al., 2022](#)). CORALv2 has had the following modifications made to it with respect to its first published version, v1: The adaptive interference mitigation scheme is adjusted such that interference that arises in front of the leading edge (LE) is also sensed and masked out for the least-squares fitting process. Moreover, the spurious interference gates are excluded from the computation of the misfit between the fitted, idealised and received waveform, from which the quality flag is deduced. Another modification is the consideration of the range migration correction (RMC) mode that has been activated on-board from S6-MF cycle 33 to accommodate the data volume to be transferred to the ground, which truncates the first ten and roughly the second half of each multilooked waveform (thus reducing the data rate by a factor of two) ([Donlon et al., 2021](#)). In these cases, only the range gates ranging from 11 to 132 (0-based) are fitted against the SAMOSA2 model ([EUMETSAT, 2022b](#)).

We retrack the different datasets from [Table 1](#) (apart from PDAP-HR and PDAP-LR) with CORALv2. The FFSAR-60 and FFSAR-140 are retracked in their corresponding posting rates of 60 Hz and 140 Hz, respectively. For the sake of comparability of the different datasets and the concurrent exploitation of potential gains, we reduce the FFSAR-60 and FFSAR-140 datasets to 20 Hz by taking the mean of all estimates around the location of the centre estimate, which coincides with the baseline L2 location, as defined during the multilooking process described in [Section 3.1.1](#). In the reduction process, we discard the higher posting rate estimates of 60 Hz and 140 Hz that exhibit a bad quality flag to exploit the high FF-SAR resolution.

Despite the application of the adaptive mitigation scheme of the CORALv2 retracker that tackles the interference in the across-track/range direction at its best, outliers cannot be completely avoided, irrespective of the type of L1b processing. Hence, after retracking and reducing the data, we filter out outliers by applying the scaled median absolute deviation (MAD) factor criterion ([Alvera-Azcárate et al., 2012](#); [Schlembach et al., 2020](#); [Passaro et al., 2021](#)). An estimate is seen as an outlier if its value exceeds the range of $\text{median}_{20} \pm 3 \cdot 1.4826 \cdot \text{MAD}$, where median_{20} and MAD are calculated on the adjacent 20 records, and the factor 1.4826 converts the MAD to a standard deviation equivalent for normally distributed data. In total, 743/18489 (4.0%), 716/18489 (3.9%), and 638/18489 (3.5%) SWH estimates are removed from the FFSAR-60, FFSAR-140 and UFSAR-20 datasets, respectively. The slightly higher amount of detected outliers for FFSAR-140/60 vs UFSAR-20 is expected, as FF-SAR is capable of resolving strongly reflective targets at a much finer scale, leading to isolation and detection of more outliers. In contrast, UF-SAR smears the spurious signal over multiple SWH waveforms, impeding the detection. The obtained numbers are in line with the amount of the scaled MAD criterion-detected outliers found in the Round Robin retracker comparison in [Schlembach et al. \(2020\)](#) for the baseline SAMOSA-based retracker (3%–5%) in the coastal zone with a dist-to-coast of less than 20 km.

3.2. Statistical analysis

We divide the statistical analysis into two parts: First, we compare the L2 datasets with the SWAN-Kuststrook wave model and assess Pearson's correlation coefficient, the median offset, and the percentage of

cycles for high correlation (PCHC). The correlation is a statistical measure of the linear relationship between two collocated datasets ranging from -1 to 1 . A concurrent increase/decrease in both thus yields a positive correlation. The median offset is defined as $\text{median}(\text{SWH}_{L2} - \text{SWH}_{\text{model}})$ and is chosen to determine the accuracy of the dataset with respect to the wave model. The PCHC is a statistical metric to assess the quality of the records on a per-cycle-basis, which was developed for the collocation of altimetry data with in-situ data by [Passaro et al. \(2015\)](#). It evaluates the number of cycles that show a high correlation with another collocated reference (here, we use the SWAN-Kuststrook wave model) and puts it into relation to the total number of cycles. [Schlembach et al. \(2022\)](#) assessed a correlation coefficient of 0.82 for a dist-to-coast of less than 5 km for CORALv1 vs a global ERA5-based wave model. We thus consider a correlation of ≥ 0.8 as high. The procedure for the computation of the PCHC is established iteratively: First, the correlation between all altimeter-model record pairs is computed. If it is below 0.8, the cycle with the largest absolute, accumulated difference between the collocated altimeter-model pairs is discarded. This procedure is repeated until the correlation of all remaining altimeter-model pairs is greater than or equal to 0.8. The PCHC is thus given as the ratio between the number of remaining cycles and the total number of cycles and amounts to 100% in the optimal and 0% in the worst case.

The second part of the statistical analysis evaluates the number of valid records and the L2 noise. The number of valid records is based on the quality flag, which indicates whether an estimate is good or bad and is provided as a product of the retracking algorithms by each of the L2 datasets. For the CORALv2-retracked L2 datasets FFSAR-140/60 and UFSAR-20, the quality flag is set as follows: First, the misfit is computed by the root mean squared differences between the bins of the received waveform and the idealised, fitted waveform while excluding the bins that are affected by coastal interference. If the misfit exceeds an empirical threshold value of 4, the quality flag is set bad, otherwise true. For further details, refer to [Schlembach et al. \(2022\)](#). The L2 noise is defined as the root-mean-square difference between consecutive 20 Hz measurements, written as

$$n_{L2} = \sqrt{\frac{\sum_{i=1}^{N-1} (\text{SWH}_{i+1} - \text{SWH}_i)^2}{N-1}} \quad (1)$$

where N is the number of records considered for the computation of the L2 noise.

The statistical quantities are computed as a function of dist-to-coast bands, which are chosen as follows: $0 \leq \text{dist-to-coast} < 1$ km, $1 \leq \text{dist-to-coast} < 3$ km, $3 \leq \text{dist-to-coast} < 5$ km, and $5 \leq \text{dist-to-coast} < 10$ km (short-hand-noted as 0–1, 1–3, 3–5, 5–10 km).

3.3. Coastal SWH variation

We define the change in SWH from offshore towards the coast as the coastal SWH variation. To estimate the coastal and offshore wave heights, we take the median SWH of the two coastal 1–3 km and 5–7 km and the offshore 29–31 km dist-to-coast bands, respectively. The choice of the coastal 5–7 km band and the offshore 29–31 km bands are based on the work of [Passaro et al. \(2021\)](#), where the first valid, 1 Hz SWH estimate is selected for the calculus of the coastal SWH variation after discarding the records for the first three kilometres.

The coastal SWH variation ratios Δ_{2-30} and Δ_{6-30} are given by

$$\Delta_{2-30} = \left(1 - \frac{\text{median}(\text{SWH}_{1-3})}{\text{median}(\text{SWH}_{29-31})}\right) \cdot 100 \quad (2)$$

and

$$\Delta_{6-30} = \left(1 - \frac{\text{median}(\text{SWH}_{5-7})}{\text{median}(\text{SWH}_{29-31})}\right) \cdot 100 \quad (3)$$

where SWH_{1-3} , SWH_{5-7} , and SWH_{29-31} are the SWH estimates in the 1–3 km, 5–7 km, and 29–31 km dist-to-coast bands, respectively.

We perform the coastal SWH variation analysis for passes 18, 120, and 196 only, as passes 44 and 213 do not include (collocated) data at a dist-to-coast of around 30 km.

4. Results and discussion

4.1. Statistical analysis

In this section, we present the results of the statistical analysis, which are summarised in Fig. 2. The column panels of Fig. 2 correspond to the statistic metrics: correlation, number of valid records, median offset, PCHC, and L2 noise. The row panels correspond to the statistical quantities in total and for each of the individual passes.

We first compare the altimetry datasets with the SWAN-Kuststrook wave model and assess the correlation, the median offset, and the PCHC. Secondly, we evaluate the intrinsic quantities of the number of valid records and the L2 noise.

4.1.1. Comparison with the SWAN-Kuststrook wave model

Correlation. From Fig. 2 (a), we observe the highest correlation >0.8 between the FF-SAR altimetry and wave model for up to 1 km from the coast, which indicates an increased consistency between both datasets and suggests an improvement since both datasets are independent. FF-SAR shows slightly greater similarities to the wave model than UF-SAR (1–3 km band: FFSAR-140: 0.82, UFSAR-20: 0.66). While showing a high similarity, the altimetry data might exhibit an offset with respect to the wave model. The assessment of the median offset is evaluated after the analysis of the correlation.

However, for closer than 1 km from the coast, these improvements inevitably depend on the altimeter measurement geometry and are hence more or less pronounced depending on the individual satellite track. Passes 120 and 196 show the least amount of land intrusion in the last few footprints closest to the coastline and thus show the highest correlation with the SWAN-Kuststrook wave model. Moreover, it is noticeable that both FFSAR-140/60 datasets show a better correlation than UFSAR-20 for pass 120. This might be due to the spurious interference that arises from strongly reflective targets in the along-track direction, which FF-SAR might be better capable of resolving due to its inherently high along-track resolution of ~ 1 m. This phenomenon will be presented and further discussed in Section 4.2.2.

In general, pass 44 shows deteriorated correlations between all altimetry datasets and the wave model compared to the residual passes. This indicates inaccuracies in the wave model, for which pass 44 lies at the left-most edge of the model domain where modelled data is strongly affected by the boundary conditions from the coarse-grained ECMWF-WAM model.

Median offset. With the analysis of the median offset, we address how accurately the altimetry datasets estimate SWH with respect to the SWAN-Kuststrook wave model as a function of the dist-to-coast bands. In the optimal case, no offset should be present. If this is not the case, then a constant offset for different values of dist-to-coast between both is desirable since other metrics can also be compared, e.g. the analysis of the coastal SWH variation, as presented in Section 4.3. A discussion of systematic offsets between the altimetry datasets and the wave model with respect to the open ocean segments of the study (dist-to-coast ≥ 20 km) and different sea states is given in Section 4.2.

From Fig. 2 (c), we observe that all altimetry datasets exhibit higher SWH than SWAN-Kuststrook. The FF-SAR-processed datasets exhibit, across all passes, a median offset of ~ 32 cm for up to 3 km from the coast and ~ 27 cm for closer than 3 km from the coast. UFSAR-20 shows a similar offset behaviour towards the coast but ~ 13 – 14 cm lower in magnitude. The offsets for dist-to-coast closer than 1 km from the coast are relatively constant for FF-SAR, whereas there are greater variations for UF-SAR. That is, with respect to the wave model, FF-SAR is capable of estimating SWH more accurately for closer than 1 km from the coast than UF-SAR and as accurate for up to 3 km from the coast.

The difference in offsets between FF-SAR and UF-SAR is as expected and due to the fitting of the FF-SAR-processed waveforms against the SAMOSA2 zero-Doppler beam that was generated with a so-called

unambiguous PTR approximation (European Space Agency and Noordwijk, The Netherlands, 2021). The used α_p LUT was thus generated under the assumption of an ideal PTR without considering any grating lobes (Ehlers et al., 2022), which might cause parts of the additional offset. Another part of the offset might be caused by the fitting of the SAMOSA2 zero-Doppler beam itself and the stronger dependence of FF-SAR on vertical wave velocities (Buchhaupt et al., 2021). If the sea surface were static, then the SAMOSA2 zero-Doppler beam waveform would be an appropriate model function (Ehlers et al., 2022). With increasing vertical velocities, the scatterers' signal is moved in the along-track direction and smeared in range such that the waveforms are widened, which causes an overestimation of SWH.

Percentage of cycles with high correlation. The PCHC represents the ratio of the cycles that show a high correlation of greater than or equal to 0.8 and the total number of cycles, as described in Section 3.2. In Fig. 2 (d), the PCHC across all passes is shown. The PCHC is related to the correlation shown in the left panels of Fig. 2, which is evaluated over all collocated altimeter-wave model records, whereas the PCHC considers the correlations of the collocations cycle-wise. That is, if the correlation values of a dist-to-coast band are close to 0.8, the PCHC value will also be high, as some cycles might exceed a correlation value of 0.8, while others do not. If all cycles exceed a correlation of at least 0.8, the PCHC value will be 100%.

We observe that up to 3 km from the coast, all CORALv2-retracked datasets show that all cycles are highly correlated, i.e. with correlations of ≥ 0.8 (apart from pass 44, from which we assume that the wave model is inaccurate). Approaching the coast yields a decrease in correlation, which corresponds to a decrease in the PCHC. FF-SAR shows, across all passes, higher PCHC values in the 1–3 km dist-to-coast band than UFSAR-20 (100% vs 76%), which is due to pass 213 whose footprints are highly affected by strongly reflective targets such as sandbanks. The PCHCs of the 0–1 km dist-to-coast band vary strongly between the individual passes, which is caused by the varying correlations of each pass. For passes 18 and 44, UF-SAR shows higher PCHCs, which might be due to the scarcity of available records in this dist-to-coast band. In the residual passes, the FF-SAR variants show the highest PCHC scores and, thus, the highest degree of similarity with the SWAN-Kuststrook wave model.

4.1.2. Number of valid records and precision

The number of valid records and the precision, defined as L2 noise, of the altimetry data are analysed, as described in Section 3.2. Both metrics do not require any external data and serve as complementary metrics for the statistical analysis vs the SWAN-Kuststrook wave model. Both measures have a substantial impact on the uncertainty of the estimates. A higher number of valid records yields more independent measurements to reduce the overall uncertainty and allows us to resolve features, such as spatial gradients in SWH when approaching the coastline, at smaller scales. Lower L2 noise values are a direct measure of the variability of the along-track estimates and likewise correspond to a lower uncertainty for each of the estimates.

Number of valid records. For up to 3 km from the coast, 95%–100% are seen as good estimates for all CORALv2-retracked products across all passes. For a dist-to-coast closer than 3 km, FF-SAR exhibits more valid estimates than UF-SAR (1–3 km band: FFSAR-140: 79%, UFSAR-20: 49%). That is, FF-SAR better resolves spatial gradients in SWH and exhibits lower uncertainties, which is shown in the coastal SWH variations, as presented in Section 4.3.

The dependency on individual passes can also be seen in the number of valid records. They are coupled with the correlation of the passes, i.e. passes that show a deteriorated correlation likewise exhibit a decreased number of valid records in the corresponding dist-to-coast bands (e.g. pass 18, 0–1 km; pass 44, 1–3 km; pass 213, 1–3 km).

The number of valid records strongly depends on the passes and thus on the angle of approach of the satellite towards the coastline.



Fig. 2. Statistical analysis of the SWH estimates for the FFSAR-60, FFSAR-140, UFSAR-20, and PDAP-HR datasets for all and each of the individual passes. The column panels show the Pearson correlation coefficients, the number of valid records, the median offset, PCHC and L2 noise in the dist-to-coast bands 0–1, 1–3, 3–5, and 5–10 km, respectively. The row panels of the plots correspond to all passes, pass 18, 44, 120, 196, and 213, respectively.

The more the footprints in front of the coastline are affected by land intrusion, the fewer records are indicated as good estimates, and at the same time, show a deteriorated correlation with the wave model. For instance, this can be observed for pass 120, whose footprints are least affected by land (see Fig. 1 (d)) and which shows the highest number of valid records with the highest correlation. In contrast, pass 213, whose footprints are strongly affected by sandbanks and land (see Fig. 1 (f)), shows reduced numbers of estimates (FFSAR-140: 41%–66%) and decreased correlations (FFSAR-140: 0.69/0.84 for the 0–1/1–3 bands).

L2 noise. The rightmost column panels of Fig. 2 show the estimated L2 noise of the datasets, as described in Section 3.2. Moreover, Fig. 3 shows, in addition, the furthest offshore dist-to-coast band of 10–30 km and the gain in precision from FFSAR-140 to UFSAR-20 (difference of L2 noise values).

The gain in precision between FF-SAR and UF-SAR is remarkable. Between FFSAR-140 and UFSAR-20, it amounts to 11–15 cm throughout the dist-to-coast bands, corresponding to a relative gain of 29%–43%. The differences between the two FF-SAR variants are

not significant. When approaching the coastline from offshore to the coastline, the L2 noise gradually increases from ~20 cm at 10–30 km to ~30 cm at 1–3 km from the coast, which is attributed to individual estimates that are affected by coastal interference.

With respect to the individual passes, we find that the L2 noise level slightly varies: Pass 120, with the least intrusion of land, shows no significant increase in noise up to the coastline. Other passes that are more affected by land and strongly reflective targets, such as 196 and 213, show an increased noise level for a dist-to-coast of less than 3 km.

The noise level estimates that we find here are in line with the ones that were estimated for the UF-SAR retracking algorithms and S3 in Schlembach et al. (2020). Although they were estimated for a very large dataset and on the basis of the standard deviation of twenty 20 Hz measurements along a 1 Hz along-track distance, they likewise range for average sea states from 30–35 cm and >40 cm for the open ocean and the coastal zone, respectively.

In the rest of this work, we proceed with the analysis of the FFSAR-140 and UFSAR-20 datasets for the sake of simplicity.

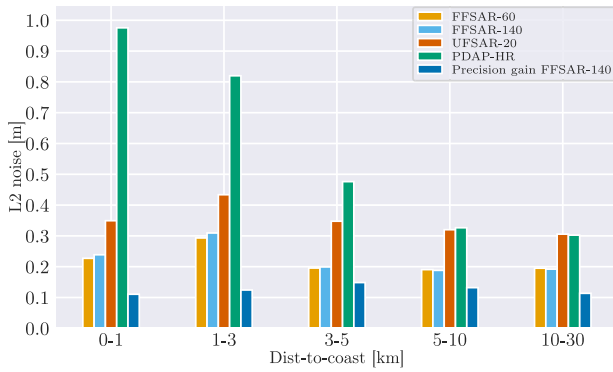


Fig. 3. L2 noise for the different dist-to-coast bands, as shown in Fig. 2 (e), but ranging from offshore at 10–30 km down to 0–1 km. In addition, the gain in precision of FFSAR-140 over UFSAR-20 is shown computed as the difference of the L2 noise values of FFSAR-140 and UFSAR-20.

4.2. Dissimilarities between altimetry and the SWAN-Kuststrook wave model

In this section, we investigate the dissimilarities between the altimetry datasets and the SWAN-Kuststrook wave model. We first analyse systematic offsets between both and then look at a specific case where we observe an increase in SWH in the last 1–2 km from the coast.

4.2.1. Systematic offsets

In the statistical analysis in Section 4.1.1, we find offsets between the altimetry data and the SWAN-Kuststrook wave model that are mostly positive, i.e. the altimetry datasets systematically overestimate SWH with respect to the wave model. As described in Section 2.2, the validation of the SWAN-Kuststrook wave model was performed in a hindcast-based analysis of four extreme events against over 50 in-situ sites, which showed only a small relative bias of $\sim 1\%$.

The sea-state-dependent overestimation of SAR-derived SWH with respect to in-situ and conventional LRM-processed altimetry data has been shown by Moreau et al. (2017, 2018), and Abdalla et al. (2018) for CS2 and in Moreau et al. (2017) and Raynal et al. (2018) for S3. Since then, it has been shown that the effect is less apparent for longer-period (swell) waves and mainly comes from wave motions (Amarouche et al., 2019; Egido and Smith, 2019; Buchhaupt, 2019). According to the S6-MF mission performance working group, the bias between the PDAP-HR and the PDAP-LR products of the EUMETSAT baseline F06 are linked to vertical wave velocities, which shows ~ 10 cm higher SWH for $\text{SWH} = 1$ m, and ~ 20 cm higher SWH for $\text{SWH} = 2$ m (EUMETSAT, 2022a; Martin-Puig et al., 2022). In Section 4.1.1, an additional offset between FF-SAR and UF-SAR found to amount to 13–14 cm. Parts of this mismatch are believed to be linked to different sensitivity of FF-SAR and UF-SAR to vertical wave motion (Buchhaupt et al., 2021). To account for the effect of vertical wave motions and the induced SWH bias, a LUT was proposed by Egido et al. (2022) that applies a sea-state-dependent SWH correction, which is planned to become operational for S6-MF baseline F09 in Q3 2023 (Scharroo et al., 2022). More recently, Buchhaupt et al. (2022) found that the HR-LR inconsistencies also originate from horizontal surface velocities that are caused by current, wind-induced movement, and swells and propose a 2D retracking scheme, which is capable of estimating both vertical wave-particle and along-track surface velocities along with the other three geophysical estimates. Based on simulations shown in Buchhaupt et al. (2022, Slide 27), the SWH bias due to horizontal surface velocities amounts to up to 4.5 cm, depending on the wind speed.

The effect of vertical wave velocities are similarly represented in our analysis: The offsets of the altimetry datasets, including the PDAP-LR product to SWAN-Kuststrook, are shown as a function of SWAN-Kuststrook SWH in Fig. 4 (a), which exhibit a dependency on the sea state. SWAN-Kuststrook underestimates the SWH with respect to the PDAP-LR product by about 5–10 cm in the range of SWH values, which is relatively constant for an SWH of up to 2 m (in between most of the SWAN-Kuststrook estimates range). The magnitude of the offset between the PDAP-HR and PDAP-LR datasets is within the range that is shown in EUMETSAT (2022a, Figure 3). The stronger variations of SWH offsets of larger than 2 m likely arise due to the fewer estimates in this sea state region, which yields a poorer statistical representation.

Fig. 4 (b) shows the probability density function (PDF) of the SWAN-Kuststrook SWH in the offshore part of the considered area (dist-to-coast ≥ 20 km), showing a median SWH of 1.08 m (5% percentile: 0.40 m, 95% percentile: 2.52 m). Fig. 4 (c) compares the PDFs of the offshore SWH values of FFSAR-140 and UFSAR-20 including the corresponding median SWH value. The offset between the medians of FFSAR-140/UFSAR-20 and SWAN-Kuststrook is in line with the results of Fig. 4 (a) (1.47 m/1.37 m vs 1.08 m), as well as the relative difference between FFSAR-140 and UFSAR-20 (~ 10 cm). Few values of $\sim 1.5\%$ of the UFSAR-20 are located in the smallest bin, potentially caused by suboptimal estimations determined by the lower SWH boundary during the iterative fitting of the retracking procedure. FFSAR-140 is unaffected by this due to the positive offset regarding UFSAR-20. Fig. 4 (d) depicts the median offset of the 5–10 km, 10–20 km, and 20–30 km dist-to-coast bands. The median offsets of the 20–30 km band amount to 42 cm and agree with the ones that can be seen from the differences between SWAN-Kuststrook and the individual datasets in Fig. 4 (a), considering a median SWH of ~ 1.0 . The quality of the PDAP-LR estimates is too poor to analyse the nearshore offsets closer than 10 km from the coast.

4.2.2. Increase in significant wave height estimates

We find that a significant number of the individual overpasses show increasing SWH estimates in the last 1–2 km from the coast, as depicted exemplarily in Fig. 5 (b) for the overpass of cycle 40 and pass 120. The increase is apparent for both the FFSAR-140 and UFSAR-20 datasets, while it is more significant for UFSAR-20 in both the intensity (SWH increase from below 0.5 m to almost 1.5 m) and the dist-to-coast of ~ 2 km. For FFSAR-140, the increase in SWH is up to ~ 0.9 m, and it stretches to ~ 1.5 km off the coast. The reason for the increase is explained by an extraordinarily strong reflective target, which is the straight sandbank at the defined coastline of pass 120 and the absence of any other land intrusions within the footprint, as shown in Fig. 5 (a). This is visualised by the multilooked echo power radargram in Fig. 5 (c) and (d) for FF-SAR and UF-SAR (with a posting rate of 140 Hz), respectively. The grating lobes of the S6-MF along-track PTR (Ehlers et al., 2022, Figure 6, Panel F), which are induced by the strong signal components of the sandbank interferer, can be well identified at distances of multiples of ~ 300 m off the coastline. The bow-tie-like pattern can also be recognised as the power is increasingly smeared over more range gates for waveforms that are further away from the sandbank. The power of the closely located grating lobes is concentrated more in the LE of the waveforms at range gates around bin ~ 100 . This strongly deteriorates the SWH estimates in the first 1–2 km off the coast.

To determine how many overpasses are affected by an increase in SWH in the last three kilometres from the coast, we apply the following empirical constraint:

$$\max(\text{SWH}_{0-3}) > \max(\text{SWH}_{3-5} + n_{1,2}) \quad (4)$$

where $\text{SWH}_{0-3/3-5}$ are the estimated SWH records for the 0–3/3–5 km dist-to-coast bands and $n_{1,2}$ the estimated L2 noise, being set to 0.2 m and 0.3 m for FF-SAR and UF-SAR and 0 for SWAN-Kuststrook, respectively.

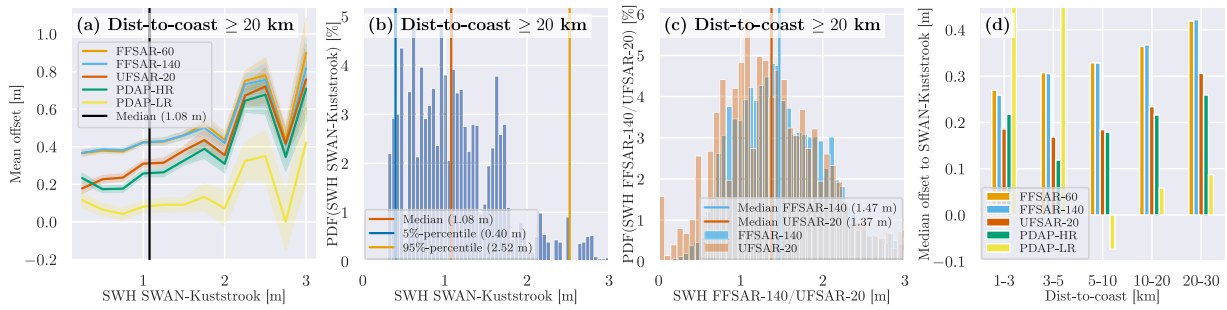


Fig. 4. The offset in the open ocean (with dist-to-coast ≥ 20 km) of the processed L2 datasets against the PDAP-LR dataset is shown in (a) as a function of the SWH from SWAN-Kuststrook, with the median offshore SWH of 1.03 m from (b). The uncertainty of the mean of each of the bins is given based on the 95% confidence interval. In (b), the PDF of the SWAN-Kuststrook SWH values is displayed with the median and the 5%- and the 95%-percentile as vertical lines. (c) compares the PDFs of the offshore SWH values of FFSAR-140 and UFSAR-20 including the corresponding median SWH value. (d) shows the evolution of the offsets of the individual datasets vs the SWAN-Kuststrook wave model from offshore at 30 km up to 1 km from the coast.

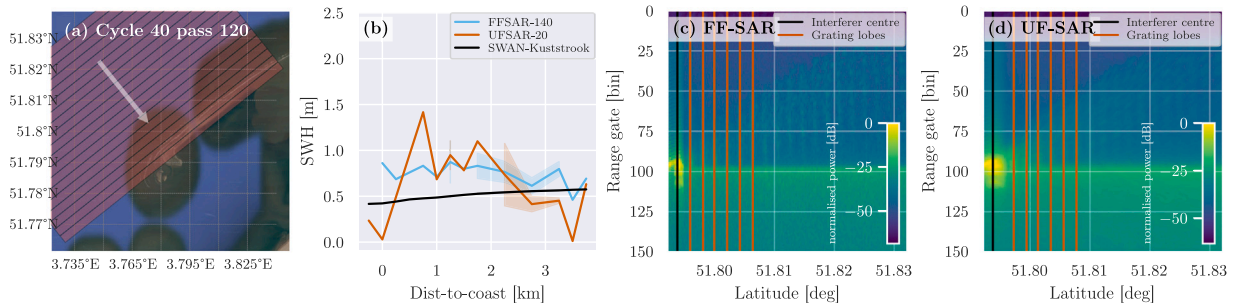


Fig. 5. (a) shows a satellite image with the effective radar footprints (corresponding to a posting rate of 20 Hz) and the strongly reflective, straight sandbank, which is crossed perpendicularly by the satellite track. The resulting retracked SWH estimates of the FFSAR-140 and UFSAR-60 datasets and SWAN-Kuststrook are shown in (b) as a function of dist-to-coast for the overpass of cycle 40, pass 120 (the shaded area of the panel indicates the 95% confidence interval of dist-to-coast bins with multiple values). The multitlooked echo power radargrams (after the L1b processing) are shown in (c) for FF-SAR and (d) UF-SAR (both with a posting rate of 140 Hz). The centre of the strongly reflective sandbank interferer and the induced grating lobes are shown at distances of multiples of ~ 300 m from the coast as vertical lines.

We apply Eq. (4) to the 138 overpasses (excluding pass 44) for the FFSAR-140 and UFSAR-20 datasets and compute the (sample) mean probability of occurrence of an SWH increase for each of the individual passes, which is shown in Fig. 6. FFSAR-140 tends to be less affected by the SWH increase. However, the margin of error, corresponding to a 95% confidence interval, is quite large, with up to 17.5%, and hence no safe conclusion can be drawn for passes 18, 196, and 213. Pass 120, though, represents an exception, as FFSAR-140 shows a strongly reduced mean probability for an SWH increase of $9.7\% \pm 10.4\%$, as compared to UF-SAR with $52.8\% \pm 17.2\%$. The SWAN-Kuststrook wave model shows an increase of (only) up to 8 cm for one overpass of passes 18 and 120, none for pass 196, and in $19.4\% \pm 6.2\%$ of the overpasses for pass 213.

A check for an increasing SWH in SWAN-Kuststrook ($\max(\text{SWH}_{0-3}) > \max(\text{SWH}_{3-5})$) reveals an increase of up to 8 cm for 10 out of the 138 cycles ($6.5\% \pm 4.1\%$), whereas pass 213 is affected most (8), and passes 18 and 120 only once.

4.3. Coastal SWH variation

The computed mean coastal SWH variations Δ_{6-30} and Δ_{2-30} of the FFSAR-140 and UFSAR-20 datasets for the passes 18, 120, and 196 are shown in Fig. 7 (a) and (b), respectively. We exclude overpasses, where SWAN-Kuststrook exhibits low sea states of less than 0.5 m around 30 km from the coast. We justify this since the poor resolution of the leading edge for very low sea states negatively affects the capability of altimeters to estimate SWH in these cases (Smith and Scharroo, 2015). Moreover, the uncertainties (precision) of the two coastal and offshore SWH values propagate through to the ratio of both values (Ku et al., 1966). If both are small, the uncertainty of the ratio becomes very large. These overpasses would yield unrealistic estimates for the coastal SWH

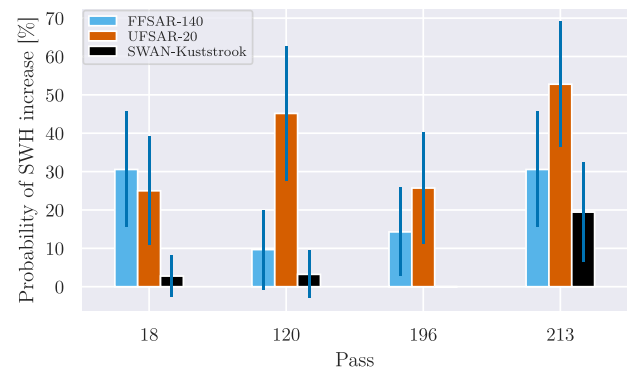


Fig. 6. Mean probabilities of occurrence for an SWH increase from 3–5 km to 0–3 km from the coast by applying Eq. (4). The error bars indicate a 95% confidence interval.

variation. In total, 15/105 low-sea-state overpasses are excluded from this analysis.

All coastal SWH variations are positive, i.e. the SWH decays towards the coastline. We observe that both FF-SAR and UF-SAR estimate the decays with respect to the 5–7 km band with no significant differences. In the 5–7 km band, both FFSAR-140 and UFSAR-20 datasets are close to the decays that are estimated by SWAN-Kuststrook (FFSAR-140: $17.4\% \pm 2.5\%$, SWAN-Kuststrook: $15.9\% \pm 2.2\%$).

However, there are more significant differences between FF-SAR and UF-SAR for the 1–3 km band: UFSAR-20 strongly underestimates the mean decay for pass 18 and also shows a large standard errors that imply a large uncertainty of the estimated variations. FFSAR-140 is, in

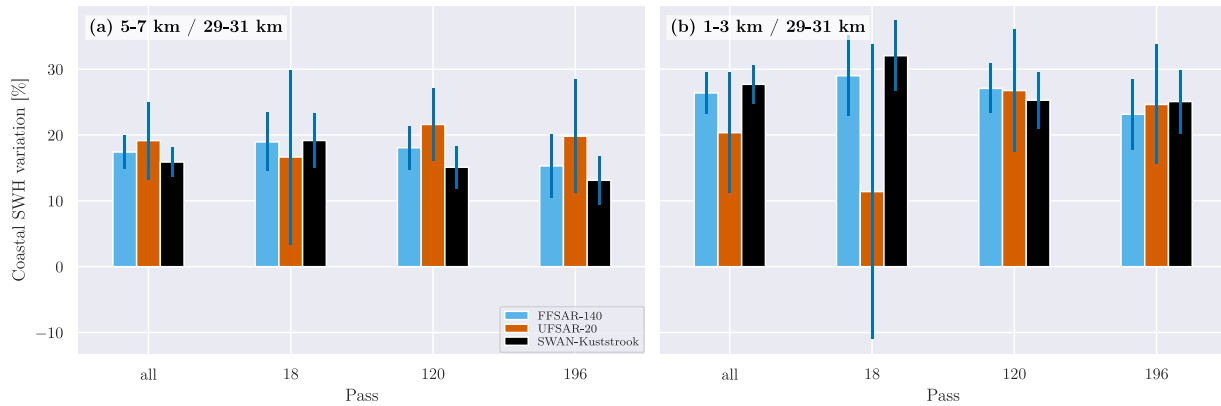


Fig. 7. Mean coastal SWH variations between the SWH between the 29–31 km dist-to-coast band and the 5–7 km or the 1–3 km dist-to-coast bands in (a) and (b), respectively, for the datasets FFSAR-140 and UFSAR-20. The error bars correspond to the 95% confidence interval.

contrast, very close to the decays of the wave model and shows a decay of $26.4\% \pm 3.1\%$.

We argue that the difference between FF-SAR and UF-SAR is explained by the differences in their 2D-PTRs. For UF-SAR, it is a sinc² with a 3-dB width of ~ 300 m, which causes the reflected power of a single point scatterer to be smeared in this distance in both the along- and across-track direction in a bow-tie-like pattern (Ehlers et al., 2022, Figure 3, Panel B). The 2D-PTR of FF-SAR is instead much peakier, with a width of ~ 1 m in the along-track direction, i.e. the main reflected power is integrated over a much smaller distance in the along-track direction at the actual location of the point scatterer (the minor grating lobes yield only $\sim 1\%$ of the total, reflected power) (Ehlers et al., 2022, Figure 6, Panel F). Thus, we argue that FF-SAR is better able to resolve (static) small-scale interferers and estimate SWH more accurately for a dist-to-coast of less than 3 km, despite the presence of interfering targets in the across-track direction that are also smeared along-track for UF-SAR.

Passaro et al. (2021) found that the global mean coastal SWH variation at >3 km from the coastline, corresponding to our 5–7 km dist-to-coast band, is 22% with respect to the offshore SWH at 30 km. However, strong variations have been assessed for 14 different regions of the global coastal ocean (Reguero et al., 2015), which show a mean value of $17.2\% \pm 3.4\%$. For the Northern and Western Europe region, a decay of 22.41% was evaluated, with an average offshore sea state of $SWH = 2.23$ m and most of the areas being exposed to an open ocean with a higher ratio of swells of higher wavelengths. That is, considering a lower median SWH value of 1.03 m (from Fig. 4) and the exposure of the milder North Sea, the overall variation we have estimated with the FFSAR-140 dataset is for the 5–7 km dist-to-coast band within an expected range of $17.4\% \pm 2.5\%$.

5. Conclusion and future work

In this work, we have conducted an extensive coastal case study to assess the applicability of FF-SAR-processed S6-MF coastal altimetry data to obtain SWH estimates as close as possible to the coast. No comparable study has been performed in the past yet. The data included 161 overpasses from five passes, covering the Dutch coast and the German coast along the East Frisian Islands in the North Sea, and 38 cycles, corresponding to the year 2021. Two FF-SAR-processing configurations with the 60/140 Hz L1b posting rates and one UF-SAR processing configuration, UFSAR-20, with a 20 Hz L1b posting rate were used to process L1a data from EUMETSAT to acquire SWH estimates after the retracking process with the coastal retracking algorithm CORALv2. Once the 60/140 Hz FF-SAR datasets have been retracked, they are reduced to form 20 Hz estimates by averaging the estimates for which the quality flag indicates a good estimate. This allows the high along-track resolution of FF-SAR to be exploited.

The processed altimetry datasets, and the baseline PDAP-HR product from EUMETSAT, were compared with the coastal, high-resolution SWAN-Kuststrook wave model from the operational RWsOS operational forecasting system to assess the performance of the altimetry datasets. We observe that accurate and precise SWH records can be estimated in the nearshore zone within 1–3 km from the coast using satellite SAR altimetry. This confirms the finding of recent studies that SAR altimetry can obtain coastal estimates at much higher quality of records when compared to LRM altimetry (Dinardo et al., 2018; Schlembach et al., 2020; Dinardo et al., 2020; Gou and Tourian, 2021) and moreover demonstrates the ability to measure SWH even closer than 3 km from the coastline.

The FFSAR-140 dataset exhibits the highest similarity to the model, showing a correlation coefficient of ~ 0.8 at 45% of valid records for the 0–1 km band and 80% of valid records for the 1–3 km band. All passes, except pass 44, where the model might give inaccurate estimates, show PCHC scores of 100% from 1 km off the coast, i.e. for all cycles, a correlation coefficient of greater than or equal to 0.8 is estimated. We notice a dependence of the performance metrics on the individual passes, which are deteriorated for those where the radar footprints are highly affected by strongly reflective targets such as sandbanks and human-made infrastructure (e.g. pass 213). Such scenarios remain challenging despite the application of FF-SAR altimetry and represent a limitation for satellite altimetry in the nearshore zone. The baseline PDAP-HR product shows strongly deteriorated correlations and a smaller number of valid records for a dist-to-coast of less than 10 km, e.g. a correlation of ~ 0.45 at $\sim 50\%$ of valid records for the 1–3 km band for all passes. We have observed that the correlation and number of valid records can be further improved if the L1b posting rate is increased for the FF-SAR-variants from 60 to 140 Hz without any sacrifice in precision. We noticed offsets between the FF-SAR- and UF-SAR-processed datasets, which might to a certain fraction be caused by vertical wave velocities that have a different influence for FF-SAR processing (Buchhaupt et al., 2021). With increasing vertical velocities, the scatterers' signal is moved in the along-track direction and smeared in range such that the waveforms are widened, which causes an overestimation of SWH (Ehlers et al., 2022).

The FF-SAR datasets show an L2 noise of ~ 20 cm in the open ocean segments and ~ 31 cm for closer than 3 km from the coast, whereas UFSAR-20 exhibits L2 noise levels of ~ 31 cm and ~ 43 cm, respectively. That is, FF-SAR achieves a gain in precision of $\sim 37\%$ and up to $\sim 29\%$ in the open ocean and closer than 3 km off the coast. The PDAP-HR product shows similar L2 noise values as UFSAR-20 for more than 5 km from the coast, and increasingly higher values towards the coast of more than 82% for closer than 3 km off the coast, respectively.

We have also identified dissimilarities between estimates of the altimetry datasets and the SWAN-Kuststrook, which are mainly a consequence of known issues related to SAR altimetry parameter estimation;

see references in Section 4.2. Accordingly, we observed that all FF-SAR- and UF-SAR-processed datasets exhibit a positive offset with respect to the wave model with a median offset of 34 cm (5%-percentile: 17 cm; 95%-percentile: 66 cm). Major parts of the offset are known and are likely caused by the influence of vertical wave velocities that are specific to SAR altimetry processing (FF-SAR more than UF-SAR) (Buchhaupt et al., 2021). This has been shown by including the PDAP-LR from the baseline L2 product in the offset analysis. A much smaller offset of less than 10 cm was observed between the PDAP-LR dataset and the SWAN-Kuststrook wave model for low and average sea states of up to 2.0 m in SWH. The median offset to the model gradually decreases from ~42 cm for 20–30 km from the coast to ~26 cm for less than 1 km off the coast (for FFSAR-140).

In order to exploit the nearshore SWH estimates of the altimetry dataset, we have investigated the coastal SWH variations, which quantify the change in SWH from offshore at 30 km to the two coastal dist-to-coast bands 5–7 km and 1–3 km. With the FFSAR-140 dataset, we observed a mean decay in SWH of $17.4\% \pm 2.5\%$ and $26.4\% \pm 3.1\%$ with respect to the 5–7 km and the 1–3 km dist-to-coast bands for the three S6-MF passes 18, 120, and 196. The decays for the 5–7 km band are within the expected range of the ones globally and regionally found in Passaro et al. (2021). We thus demonstrated that the FFSAR-140 processing-configuration is also capable of giving accurate estimates for the coastal SWH variation in regard to the 1–3 km band.

To summarise the results of the individual objectives of this study, we can draw the following conclusions, which have not been shown by any previous work:

FF-SAR vs UF-SAR FF-SAR SWH estimates were found to exhibit lower noise, resulting in increased correlation with the numerical wave model, and provide a higher number of valid records and highly correlated cycles, as compared to the UF-SAR estimates.

High-quality SWH estimates from 1 km from the coast This case study demonstrates that one can acquire robust high-frequency SWH estimates up to 1 km off the coast by the combination of FF-SAR altimetry, the coastal CORALv2 retracker, and the subsequent removal of residual outliers.

Estimation of nearshore, coastal SWH variations With the aforementioned FF-SAR-configuration, we are able to give accurate estimates with respect to a numerical wave model for the coastal SWH variation of up to 1 km from the coast. The approach angle of the satellite track, as well as the existence of strongly reflective targets such as sandbanks, tidal flats, calm waters or human-made infrastructure being located nearshore, are still dominating factors that influence the quality of the SWH estimates, regardless of FF-SAR-processing.

FFSAR-140 represents the processing configuration with the best performance but, at the same time, exhibits the highest amount of computational complexity. However, it must also be noted that the used FF-SAR back-projection processing methodology is not the most efficient one. Guccione et al. (2018) have proposed the omega-kappa FF-SAR processing methodology, which strongly reduces the computational efforts with negligible costs in performance.

In this work, we found that FF-SAR processing combined with a coastal retracker gives additional gains for distances of up to 1 km from the coast in terms of accuracy, precision, and availability of the SWH records. The quality of the nearshore SWH estimates varies depending on the characteristics of the individual crossing of the shoreline, and thus on the existence of strongly reflective targets within the radar footprints. As part of future work, we thus suggest the development of more advanced interference mitigation techniques, tailored to FF-SAR-processed altimetry data. The suppressing of signals from static interfering targets might give an additional gain for FF-SAR processing.

The improvement of the quality flagging after multilooking at the higher posting rates provides additional gains in the robustness of the L2 estimates. We also suggest studying the difference between the FF-SAR- and UF-SAR-processed datasets in more detail to be able to characterise small-scale features such as breaking waves or shoaling effects that FF-SAR might be able to resolve.

CRediT authorship contribution statement

Florian Schlembach: Conceptualization, Methodology, Software, Formal analysis, Investigation, Resources, Writing – original draft, Writing – review & editing, Visualisation. **Frithjof Ehlers:** Software, Formal analysis, Resources, Writing – review & editing. **Marcel Kleinerbrink:** Software, Resources, Writing – review & editing, Supervision. **Marcello Passaro:** Writing – review & editing, Supervision, Project administration, Funding acquisition. **Denise Dettmering:** Writing – review & editing. **Florian Seitz:** Writing – review & editing, Project administration, Funding acquisition. **Cornelis Slobbe:** Software, Resources, Writing – review & editing, Supervision.

Declaration of competing interest

The authors declare that they have no known competing financial interests or personal relationships that could have appeared to influence the work reported in this paper.

Data availability

Data will be made available on request.

Acknowledgements

The authors gratefully acknowledge Deltares for the provision of the operational SWAN-Kuststrook wave model. We would like to thank the three anonymous reviewers who helped to improve this article. Further, we would like to acknowledge the contributions of Python (Van Rossum and Drake, 2009) and the following Python packages that we used: NumPy (Harris et al., 2020), SciPy (Virtanen et al., 2020), pandas (McKinney, 2010), Matplotlib (Hunter, 2007), Cython (Behnel et al., 2011), and seaborn (Waskom, 2021).

All authors read and approved the final version of the manuscript.

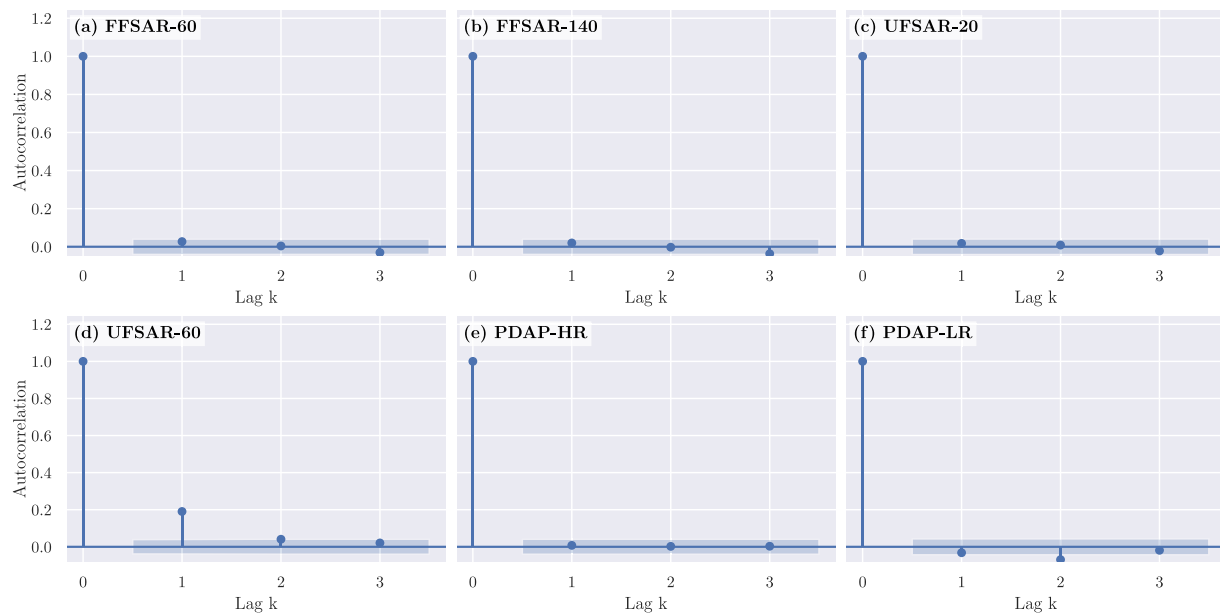
Funding

This research has been funded by the European Space Agency as part of the Sea State Climate Change Initiative (SeaState_cci) project: ESA ESRIN/Contract No. 4000123651/18/I-NB. The FF-SAR SAMOSA LUT generation was funded under ESA contract 4000118128/16/NL/AI.

Appendix A. Autocorrelation analysis

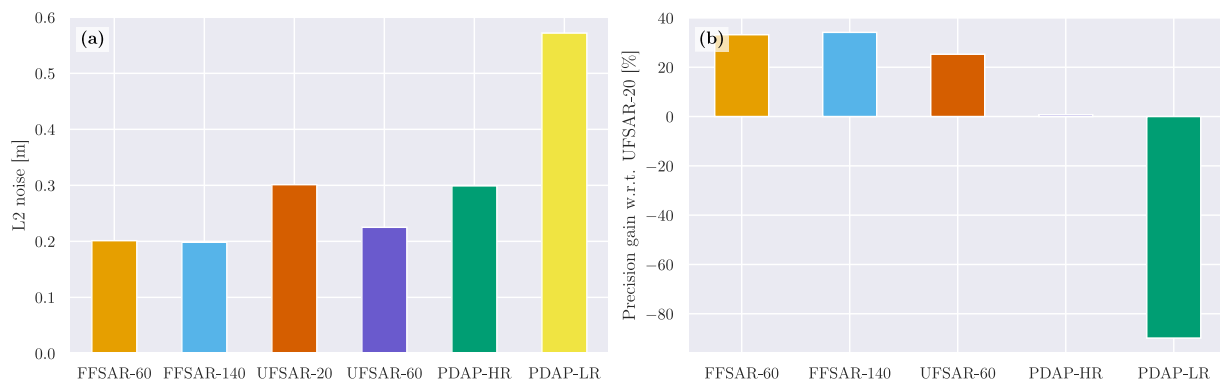
Dinardo et al. (2015) and Egidio et al. (2020) suggest increasing posting rates to more than 20 Hz as commonly used by the EUMETSAT baseline products. In this work, the authors assume that the decorrelation length of the radar echoes is much smaller in the along-track direction than the inherent unfocused synthetic aperture radar (UF-SAR) along-track resolution of ~300 m. Hence, depending on the sea state, a precision gain of 20%–30% can be achieved for the geophysical estimates if the posting rates are increased to 40 or 60 Hz and then averaged to form 20 Hz estimates.

We have analysed the autocorrelation function (ACF) of different processing options by considering open ocean segments with a distance-to-coast (dist-to-coast) between 20 km and 30 km. We exclude those that show a larger standard deviation than 20 cm, 30 cm, and 50 cm for fully focused synthetic aperture radar (FF-SAR)-, UF-SAR- and



1

Fig. A.8. Autocorrelation of the datasets FFSAR-60, FFSAR-140, UFSAR-20, UFSAR-60, PDAP-HR, and PDAP-LR in a-f, respectively. The light blue area for $k \neq 0$ indicates the standard error of white noise, which is approximated as $\sigma_n = \sqrt{N^{-1}}$, with N being the number of estimates.



1

Fig. A.9. The L2 noise of the datasets FFSAR-60, FFSAR-140, UFSAR-20, UFSAR-60, PDAP-HR, and PDAP-LR is shown in (a). The gain in precision is shown relative to UFSAR-20 in (b).

low resolution mode (LRM)-processed datasets, respectively. We have added the two datasets, UFSAR-20 and Payload Data Acquisition and Processing Low Resolution (PDAP-LR), to assess their autocorrelations. The datasets with posting rates of more than 20 Hz are arithmetically averaged to yield the targeted 20 Hz posting rate. The ACFs of the first three lags for the different datasets are shown in Fig. A.8. Apart from UFSAR-60, all datasets exhibit no correlation between their adjacent records, as the ACF stays within the confidence interval of the standard error of white noise (Brockwell and Davis, 1987). UFSAR-60 shows a correlation of ~ 0.2 for lag $k = 1$. The resulting L2 noise, or precision, and the gain in precision over UFSAR-20 are shown in Fig. A.9 (a) and (b), respectively. No correlation is observed for the FF-SAR-processed datasets, not even for FFSAR-60 and FFSAR-140. UFSAR-20 shows a gain in precision of 25.3% over PDAP-HR. This is noticeable and in line with the numbers being reported by Egido et al. (2020), who estimated precision gains of 22% and 25% for posting rates of 40 Hz and 60 Hz. Nevertheless, we find that the increased precision of the geophysical estimates is, per se, not an actual gain but comes together with an added correlation between the reduced 20 Hz estimates. The

subsampling of the 20 Hz estimates thus acts as a smoothing or low-pass filter, which smears the effective signal over the subsequent estimate. Consequently, we decided not to include any UFSAR datasets with posting rates of larger than 20 Hz in this study to allow for a fair comparison of the individual analysed datasets.

Appendix B. Supplementary data

Supplementary material related to this article can be found online at <https://doi.org/10.1016/j.rse.2023.113517>.

References

- Abdalla, S., Dinardo, S., Benveniste, J., Janssen, P.A., 2018. Assessment of CryoSat-2 SAR mode wind and wave data. *Adv. Space Res.* 62 (6), 1421–1433. <https://doi.org/10.1016/j.asr.2018.01.044>.
- Alvera-Azcárate, A., Sirjacobs, D., Barth, A., Beckers, J.-M., 2012. Outlier detection in satellite data using spatial coherence. *Remote Sens. Environ.* 119, 84–91. <https://doi.org/10.1016/j.rse.2011.12.009>.

- Amarouche, L., Tran, N., Herrera, D., 2019. Impact of the ocean waves motion on the delay/Doppler altimeters measurements. In: Ocean Surface Topography Science Team (OSTST) Meeting.
- Arens, S.M., Mulder, J.P.M., Slings, Q.L., Geelen, L.H.W.T., Damsma, P., 2013. Dynamic dune management, integrating objectives of nature development and coastal safety: Examples from the Netherlands. *Geomorphology* 199, 205–213. <http://dx.doi.org/10.1016/j.geomorph.2012.10.034>.
- Behnel, S., Bradshaw, R., Citro, C., Dalcin, L., Seljebotn, D.S., Smith, K., 2011. Cython: The best of both worlds. *Comput. Sci. Eng.* 13 (2), 31–39. <http://dx.doi.org/10.1109/MCSE.2010.118>.
- Booij, N., Ris, R.C., Holthuijsen, L.H., 1999. A third-generation wave model for coastal regions: 1. Model description and validation. *J. Geophys. Res.: Oceans* 104 (C4), 7649–7666. <http://dx.doi.org/10.1029/98JC02622>.
- Brockwell, P.J., Davis, R.A., 1987. Time Series: Theory and Methods. In: Springer Series in Statistics, Springer, New York, NY, <http://dx.doi.org/10.1007/978-1-4899-0004-3>.
- Bryan, K.R., Power, H.E., 2020. 4 - Wave behaviour outside the surf zone. In: Jackson, D.W.T., Short, A.D. (Eds.), *Sandy Beach Morphodynamics*. Elsevier, pp. 61–86. <http://dx.doi.org/10.1016/B978-0-08-102927-5.00004-7>.
- Buchhaupt, C., 2019. Model Improvement for SAR Altimetry (Ph.D. thesis). Schriftenreihe Fachrichtung Geodäsie der Technischen Universität Darmstadt, Darmstadt.
- Buchhaupt, C., Egido, A., Smith, W., Vandemark, D., Fenoglio-Marc, L., Leuliette, E., 2022. 2D SAR altimetry retracking – lessons learned. In: Ocean Surface Topography Science Team (OSTST) Meeting in Venice.
- Buchhaupt, C., Fenoglio, L., Becker, M., Kusche, J., 2021. Impact of vertical water particle motions on focused SAR altimetry. 25 Years of Progress in Radar Altimetry, *Adv. Space Res.* 25 Years of Progress in Radar Altimetry, 68 (2), 853–874. <http://dx.doi.org/10.1016/j.asr.2020.07.015>.
- Cavaleri, L., Fox-Kemper, B., Hemer, M., 2012. Wind waves in the coupled climate system. *Bull. Am. Meteorol. Soc.* 93 (11), 1651–1661. <http://dx.doi.org/10.1175/BAMS-D-11-00170.1>.
- Charlier, R.H., Chaineux, M.C.P., Morcos, S., 2005. Panorama of the history of coastal protection. *J. Coast. Res.* 21 (1 (211)), 79–111. <http://dx.doi.org/10.2112/03561.1>.
- Chowdhury, P., Behera, M.R., 2017. Effect of long-term wave climate variability on longshore sediment transport along Regional Coastlines. *Prog. Oceanogr.* 156, 145–153. <http://dx.doi.org/10.1016/j.pcean.2017.06.001>.
- Cipollini, P., Benveniste, J., Bouffard, J., Emery, W., Gommenginger, C., Griffin, D., Høyer, J., Madsen, K., Mercier, F., Miller, L., et al., 2009. The role of altimetry in coastal observing systems. *Proceedings of OceanObs'09: Sustained Ocean Observations and Information for Society* <http://dx.doi.org/10.5270/OceanObs09.cwp.16>.
- Cipollini, P., Benveniste, J., Miller, L., Picot, N., Scharroo, R., Strub, T., 2012. Conquering the coastal zone: A new frontier for satellite altimetry. In: 20 Years of Progress in Radar Altimetry, No. 1, pp. 3–7.
- Contardo, S., Hoeke, R., Hemer, M., Symonds, G., McInnes, K., O'Grady, J., 2018. In situ observations and simulations of coastal wave field transformation by wave energy converters. *Coast. Eng.* 140, 175–188. <http://dx.doi.org/10.1016/j.coastaleng.2018.07.008>.
- Day, C., Dietrich, J., 2022. Improved wave predictions with ST6 Physics and ADCIRC+SWAN. *Shore Beach* 59–61. <http://dx.doi.org/10.34237/1009016>.
- de Vries, S., Wengrove, M., Bosboom, J., 2020. 9 - Marine sediment transport. In: Jackson, D.W.T., Short, A.D. (Eds.), *Sandy Beach Morphodynamics*. Elsevier, pp. 187–212. <http://dx.doi.org/10.1016/B978-0-08-102927-5.00009-6>.
- Dinardo, S., Fenoglio-Marc, L., Becker, M., Scharroo, R., Fernandes, M.J., Staneva, J., Grayek, S., Benveniste, J., 2020. A RIP-based SAR retracker and its application in North East Atlantic with Sentinel-3. *Adv. Space Res.* <http://dx.doi.org/10.1016/j.asr.2020.06.004>.
- Dinardo, S., Fenoglio-Marc, L., Buchhaupt, C., Becker, M., Scharroo, R., Joana Fernandes, M., Benveniste, J., 2018. Coastal SAR and PLRM altimetry in German Bight and West Baltic Sea. *Adv. Space Res.* 62, 1371–1404. <http://dx.doi.org/10.1016/j.asr.2017.12.018>.
- Dinardo, S., Scharroo, R., Benveniste, J., 2015. SAR altimetry at 80 Hz: Open Sea, coastal zone, Inland Water. In: Ocean Surface Topography Science Team Meeting.
- Donlon, C.J., Cullen, R., Giulicchi, L., Vuilleumier, P., Francis, C.R., Kuschnerus, M., Simpson, W., Bouridah, A., Caleno, M., Bertoni, R., Rancaño, J., Pourier, E., Hyslop, A., Mulcahy, J., Knockaert, R., Hunter, C., Webb, A., Fornari, M., Vaze, P., Brown, S., Willis, J., Desai, S., Desjonqueres, J.-D., Scharroo, R., Martin-Puig, C., Leuliette, E., Egido, A., Smith, W.H.F., Bonnefond, P., Le Gac, S., Picot, N., Tavernier, G., 2021. The Copernicus Sentinel-6 mission: Enhanced continuity of satellite sea level measurements from space. *Remote Sens. Environ.* 258, 112395. <http://dx.doi.org/10.1016/j.rse.2021.112395>.
- Egido, A., Buchhaupt, C., Boy, F., Maraldi, C., Emeline, C., Salvatore, D., Leuliette, E., Moreau, T., 2022. A significant wave height correction to account for vertical wave motion effects in SAR altimeter measurements. In: Ocean Surface Topography Science Team (OSTST) Meeting in Venice.
- Egido, A., Dinardo, S., Ray, C., 2020. The case for increasing the posting rate in delay/Doppler altimeters. *Adv. Space Res.* <http://dx.doi.org/10.1016/j.asr.2020.03.014>.
- Egido, A., Smith, W.H.F., 2017. Fully focused SAR altimetry: Theory and applications. *IEEE Trans. Geosci. Remote Sens.* 55 (1), 392–406. <http://dx.doi.org/10.1109/TGRS.2016.2607122>.
- Egido, A., Smith, W.H.F., 2019. Pulse-to-pulse correlation effects in high PRF low-resolution mode altimeters. *IEEE Trans. Geosci. Remote Sens.* 57 (5), 2610–2617. <http://dx.doi.org/10.1109/TGRS.2018.2875622>.
- Ehlers, F., Schlembach, F., Kleinherenbrink, M., Slobbe, C., 2022. Validity assessment of SAMOSA retracking for fully-focused SAR altimeter waveforms. *Adv. Space Res.* <http://dx.doi.org/10.1016/j.asr.2022.11.034>.
- Elfrink, B., Baldock, T., 2002. Hydrodynamics and sediment transport in the swash zone: A review and perspectives. *Coast. Eng.* 45 (3), 149–167. [http://dx.doi.org/10.1016/S0378-3839\(02\)00032-7](http://dx.doi.org/10.1016/S0378-3839(02)00032-7).
- EMODnet Bathymetry Consortium, 2018. EMODnet Digital Bathymetry (DTM 2018). <http://dx.doi.org/10.12770/18ff0d48-b203-4a65-94a9-5fd8b0ec35f6>.
- EUMETSAT, 2022a. Sentinel-6 payload data processing (PDP) processing baseline F06 - product notice. <https://www.eumetsat.int/media/48237>.
- EUMETSAT, 2022b. Sentinel-6/Jason-CS ALT level 2 product generation specification (L2 ALT PGS), version v4D.
- European Space Agency, Noordwijk, The Netherlands, 2021. Sentinel-6 L2 GPP project.
- European Space Agency, Noordwijk, The Netherlands, 2022. Copernicus sentinel-3 next generation topography (S3NG-T), mission requirements document (MRD), v0.41, draft as of 14.06.2022.
- Fenoglio-Marc, L., Fehlau, M., Ferri, L., Becker, M., Gao, Y., Vignudelli, S., 2010. Coastal sea surface heights from improved altimeter data in the Mediterranean Sea. In: International Association of Geodesy Symposia, Vol. 135, No. June 2008, pp. 253–261. http://dx.doi.org/10.1007/978-3-642-10634-7_33.
- Ferreira, Ó., Ciavola, P., Armaroli, C., Balouin, Y., Benavente, J., Río, L.D., Deserti, M., Esteves, L., Furmanczyk, K., Haerens, P., Matias, A., Perini, L., Taborda, R., Terefenko, P., Trifonova, E., Trouw, K., Valchev, N., Van Dongeren, A., Van Koningsveld, M., Williams, J., 2009. Coastal storm risk assessment in Europe: Examples from 9 study sites. *J. Coast. Res.* 1632–1636.
- Garcia, P., Granados, A., Guerra, M., Roca, M., Lucas, B., Féménias, P., 2022. The CORS processor outcomes. Improving the Coastal Ocean SSH & SWH series from the Copernicus altimetry constellation. In: Ocean Surface Topography Science Team (OSTST) Meeting in Venice.
- Gautier, C., Cairns, S., 2015. Operational wave forecasts in the Southern North Sea. In: 36th IAHR World Congress, Vol. 1.
- Glavovic, B., Dawson, R., Chow, W., Garschagen, M., Haasnoot, M., Singh, M., Thomas, A., 2022. Cross-chapter paper 2: Cities and settlements by the sea. In: Climate Change 2022: Impacts, Adaptation and Vulnerability, Contribution of Working Group II to the Sixth Assessment Report of the Intergovernmental Panel on Climate Change. Cambridge University Press, Cambridge, UK and New York, NY, USA, pp. 2163–2194. <http://dx.doi.org/10.1017/9781009325844.019>.
- Gomez-Enri, J., Cipollini, P., Passaro, M., Vignudelli, S., Tejedor, B., Coca, J., 2016. Coastal altimetry products in the Strait of Gibraltar. *IEEE Trans. Geosci. Remote Sens.* 54 (9), 5455–5466. <http://dx.doi.org/10.1109/TGRS.2016.2565472>.
- Gou, J., Tourian, M.J., 2021. RiwiSAR-SWH: A data-driven method for estimating significant wave height using Sentinel-3 SAR altimetry. *Adv. Space Res.* <http://dx.doi.org/10.1016/j.asr.2021.12.019>.
- Guccione, P., 2008. Beam sharpening of delay/Doppler altimeter data through chirp zeta transform. *IEEE Trans. Geosci. Remote Sens.* 46 (9), 2517–2526. <http://dx.doi.org/10.1109/TGRS.2008.918863>.
- Guccione, P., Scagliola, M., Giudici, D., 2018. 2D frequency domain fully focused SAR processing for high PRF radar altimeters. *Remote Sens.* 10 (12), 1943. <http://dx.doi.org/10.3390/rs10121943>.
- Harris, C.R., Millman, K.J., van der Walt, S.J., Gommers, R., Virtanen, P., Cournapeau, D., Wieser, E., Taylor, J., Berg, S., Smith, N.J., Kern, R., Picus, M., Hoyer, S., van Kerkwijk, M.H., Brett, M., Haldane, A., Fernández del Río, J., Wiebe, M., Peterson, P., Gérard-Marchant, P., Sheppard, K., Reddy, T., Weckesser, W., Abbasi, H., Gohlke, C., Oliphant, T.E., 2020. Array programming with NumPy. *Nature* 585, 357–362. <http://dx.doi.org/10.1038/s41586-020-2649-2>.
- Holthuijsen, L.H., 2007. Waves in Oceanic and Coastal Waters. Cambridge University Press, Cambridge, <http://dx.doi.org/10.1017/CBO9780511618536>.
- Hunter, J.D., 2007. Matplotlib: A 2D graphics environment. *Comput. Sci. Eng.* 9 (3), 90–95. <http://dx.doi.org/10.1109/MCSE.2007.55>.
- Janssen, P., 2011. IFS documentation – Cy3r72 operational implementation 18 May 2011 PART VII: ECMWF WAVE MODEL. ECMWF.
- Kleinherenbrink, M., Naeije, M., Slobbe, C., Egido, A., Smith, W., 2020. The performance of CryoSat-2 fully-focussed SAR for inland water-level estimation. *Remote Sensing of Environment* 237, 111589. <http://dx.doi.org/10.1016/j.rse.2019.111589>.
- Ku, H.H., et al., 1966. Notes on the use of propagation of error formulas. *J. Res. Natl. Bur. Stand. T* 70 (4), 263–273. <http://dx.doi.org/10.6028/jres.070c.025>.
- Lippmann, T.C., Brookings, A.H., Thornton, E.B., 1996. Wave energy transformation on natural profiles. *Coast. Eng.* 27 (1), 1–20. [http://dx.doi.org/10.1016/0378-3839\(95\)00036-4](http://dx.doi.org/10.1016/0378-3839(95)00036-4).
- Martin-Puig, C., Cullen, R., Desjonqueres, J.D., Leuliette, E., Maraldi, C., Meloni, M., 2022. Cal/Val activities performed by the MPWG. In: Ocean Surface Topography Science Team (OSTST) Meeting in Venice.

- McKinney, W., 2010. Data structures for statistical computing in Python. In: Proceedings of the 9th Python in Science Conference. pp. 56–61. <http://dx.doi.org/10.25080/Majora-92bf1922-00a>.
- Melville, W.K., 1996. The role of surface-wave breaking in air-sea interaction. *Annu. Rev. Fluid Mech.* 28 (1), 279–321. <http://dx.doi.org/10.1146/annurev.fl.28.010196.001431>.
- Moreau, T., Rieu, P., Aublanc, J., 2017. Investigation of SWH bias in SAR altimetry mode. In: *Ocean Surface Topography Science Team (OSTST) Meeting*.
- Moreau, T., Tran, N., Aublanc, J., Tison, C., Le Gac, S., Boy, F., 2018. Impact of long ocean waves on wave height retrieval from SAR altimetry data. *Adv. Space Res.* 62 (6), 1434–1444. <http://dx.doi.org/10.1016/j.asr.2018.06.004>.
- NASA JPL, 2020. Sentinel-6A Michael Freilich Jason-CS (sentinel-6A) | PO.DAAC / JPL / NASA. Physical Oceanography Distributed Active Archive Center (PO.DAAC), <https://podaac.jpl.nasa.gov/Sentinel-6>.
- National Georegister of the Netherlands, 2021. Bathymetrie Nederlande – Binnenwaterstraßenkontur - Data Europa EU. <https://data.europa.eu/data/datasets/adn73c4a-ef03-4785-b7f6-942e86b385f7v?locale=de>.
- Passaro, M., Fenoglio-Marc, L., Cipollini, P., 2015. Validation of Significant Wave Height From Improved Satellite Altimetry in the German Bight. *IEEE Transactions on Geoscience and Remote Sensing* 53 (4), 2146–2156. <http://dx.doi.org/10.1109/TGRS.2014.2356331>.
- Passaro, M., Hemer, M.A., Quartly, G.D., Schwatke, C., Dettmering, D., Seitz, F., 2021. Global Coastal attenuation of wind-waves observed with radar altimetry. *Nature Commun.* 12 (1), 3812. <http://dx.doi.org/10.1038/s41467-021-23982-4>.
- Peng, F., Deng, X., 2018. A new retracking technique for brown peaky altimetric waveforms. *Mar. Geod.* 41 (2), 99–125. <http://dx.doi.org/10.1080/01490419.2017.1381656>.
- Pilarczyk, K.W. (Ed.), 1990. Coastal protection. In: *Coastal Protection: Proceedings of the Short Course on Coastal Protection*. Delft University of Technology, 30 June - 1 July 1990, Balkema, Rotterdam.
- Raney, R., 1998. The delay/Doppler radar altimeter. *IEEE Trans. Geosci. Remote Sens.* 36 (5), 1578–1588. <http://dx.doi.org/10.1109/36.718861>.
- Ray, C., Martin-Puig, C., Clarizia, M.P., Ruffini, G., Dinardo, S., Gommenginger, C., Benveniste, J., 2015. SAR altimeter backscattered waveform model. *IEEE Trans. Geosci. Remote Sens.* 53 (2), 911–919. <http://dx.doi.org/10.1109/TGRS.2014.2330423>.
- Raynal, M., Moreau, T., Tran, N., 2018. Assessment of the SARM processing sensitivity to swell. In: *Ocean Surface Topography Science Team (OSTST) Meeting*.
- Reguero, B.G., Losada, I.J., Méndez, F.J., 2015. A global wave power resource and its seasonal, interannual and long-term variability. *Appl. Energy* 148, 366–380. <http://dx.doi.org/10.1016/j.apenergy.2015.03.114>.
- Rogers, W.E., Babanin, A.V., Wang, D.W., 2012. Observation-consistent input and whitecapping dissipation in a model for wind-generated surface waves: Description and simple calculations. *J. Atmos. Ocean. Technol.* 29 (9), 1329–1346. <http://dx.doi.org/10.1175/JTECH-D-11-00092.1>.
- Sajjad, M., Chan, J.C.L., 2019. Risk assessment for the sustainability of coastal communities: A preliminary study. *Sci. Total Environ.* 671, 339–350. <http://dx.doi.org/10.1016/j.scitotenv.2019.03.326>.
- Scagliola, M., Recchia, L., Maestri, L., Giudici, D., 2021. Evaluating the impact of range walk compensation in delay/Doppler processing over Open Ocean. 25 Years of Progress in Radar Altimetry, *Adv. Space Res.* 25 Years of Progress in Radar Altimetry, 68 (2), 937–946. <http://dx.doi.org/10.1016/j.asr.2019.11.032>.
- Scharroo, R., Martin-Puig, C., Meloni, M., Nogueira Loddó, C., Grant, M., Lucas, B., 2022. Sentinel-6 products status. In: *Ocean Surface Topography Science Team (OSTST) Meeting in Venice*.
- Schlembach, F., Passaro, M., Dettmering, D., Bidlot, J., Seitz, F., 2022. Interference-sensitive coastal SAR altimetry retracking strategy for measuring significant wave height. *Remote Sensing of Environment* 274, 112968. <http://dx.doi.org/10.1016/j.rse.2022.112968>.
- Schlembach, F., Passaro, M., Quartly, G.D., Kurekin, A., Nencioli, F., Dodet, G., Piollé, J.-F., Arduin, F., Bidlot, J., Schwatke, C., Seitz, F., Cipollini, P., Donlon, C., 2020. Round robin assessment of radar altimeter low resolution mode and delay-Doppler retracking algorithms for significant wave height. *Remote Sens.* 12 (8), 1254. <http://dx.doi.org/10.3390/rs12081254>.
- Smith, W.H., Scharroo, R., 2015. Waveform aliasing in satellite radar altimetry. *IEEE Trans. Geosci. Remote Sens.* 53 (4), 1671–1682. <http://dx.doi.org/10.1109/TGRS.2014.2331193>.
- Stopa, J.E., Arduin, F., Girard-Arduin, F., 2016. Wave climate in the Arctic 1992–2014: Seasonality and trends. *Cryosphere* 10 (4), 1605–1629. <http://dx.doi.org/10.5194/tc-10-1605-2016>.
- Timmermans, B., Shaw, A.G.P., Gommenginger, C., 2020. Reliability of extreme significant wave height estimation from satellite altimetry and in situ measurements in the coastal zone. *J. Mar. Sci. Eng.* 8 (12), 1039. <http://dx.doi.org/10.3390/jmse8121039>.
- Undén, P., Rontu, L., Jarvinen, H., Lynch, P., Calvo Sánchez, F.J., Cats, G., Cuxart, J., Eerola, K., Fortelius, C., García-Moya, J.A., Jones, C., Lenderink, G., McDonald, A., McGrath, R., Navasqués, B., Woetman-Nielsen, N., Odegaard, V., Rodríguez Camino, E., Rummukainen, M., Room, R., Sattler, K., Hansen Sass, B., Savijärvi, H., Wichers Schreur, B., Sigg, R., Han, T., Tijn, A., 2002. HIRLAM-5 Scientific Documentation. Swedish Meteorological and Hydrological Institute.
- Van Rossum, G., Drake, F.L., 2009. Python 3 Reference Manual. CreateSpace, Scotts Valley, CA.
- Vignudelli, S., Kostianoy, A.G., Cipollini, P., Benveniste, J., 2011. Coastal altimetry. <http://dx.doi.org/10.1007/978-3-642-12796-0>.
- Virtanen, P., Gommers, R., Oliphant, T.E., Haberland, M., Reddy, T., Cournapeau, D., Burovski, E., Peterson, P., Weckesser, W., Bright, J., van der Walt, S.J., Brett, M., Wilson, J., Millman, K.J., Mayorov, N., Nelson, A.R.J., Jones, E., Kern, R., Larson, E., Carey, C.J., Polat, İ., Feng, Y., Moore, E.W., VanderPlas, J., Laxalde, D., Perktold, J., Cimrman, R., Henriksen, I., Quintero, E.A., Harris, C.R., Archibald, A.M., Ribeiro, A.H., Pedregosa, F., van Mulbregt, P., SciPy 1.0 Contributors, 2020. SciPy 1.0: Fundamental algorithms for scientific computing in Python. *Nature Methods* 17, 261–272. <http://dx.doi.org/10.1038/s41592-019-0686-2>.
- Wang, P., Kraus, N.C., 2005. Beach profile equilibrium and patterns of wave decay and energy dissipation across the Surf Zone Elucidated in a large-scale laboratory experiment. *J. Coast. Res.* 2005 (213), 522–534. <http://dx.doi.org/10.2112/03-003.1>.
- Waskom, M.L., 2021. Seaborn: Statistical data visualization. *J. Open Source Softw.* 6 (60), 3021. <http://dx.doi.org/10.21105/joss.03021>.
- Wright, L.D., 1976. Nearshore wave-power dissipation and the coastal energy regime of the Sydney-Jervis Bay region, New South Wales: A comparison. *Mar. Freshwater Res.* 27 (4), 633–640. <http://dx.doi.org/10.1071/mf9760633>.